Characterizing Microstructural Tissue Properties in Multiple Sclerosis with Diffusion MRI at 7 T and 3 T: The Impact of the Experimental Design

Silvia De Santis, [a]* Matteo Bastiani, [b] Amgad Droby, [d] Pierre Kolber, [d] Frauke Zipp, [d] Eberhard Pracht, [e] Tony Stoecker, [e] Sergiu Groppa [d] and Alard Roebroeck [c]

[a] *Istituto de Neurociencias de Alicante, Alicante, Spain*

[b] *Wellcome Centre for Integrative Neuroimaging – Oxford Centre for Functional Magnetic Resonance Imaging of the Brain (FMRIB), University of Oxford, UK*

[c] *Dept. of Cognitive Neuroscience, Faculty of Psychology & Neuroscience, Maastricht University, Maastricht, Netherlands*

[d] *Department of Neurology and Neuroimaging Center (NIC) of the Focus Program Translational Neuroscience (FTN), University Medical Center of the Johannes Gutenberg University Mainz, Mainz, Germany*

[e] *German Center for Neurodegenerative Diseases, Bonn, Germany*

Abstract—The recent introduction of advanced magnetic resonance (MR) imaging techniques to characterize focal and global degeneration in multiple sclerosis (MS), like the Composite Hindered and Restricted Model of Diffusion, or CHARMED, diffusional kurtosis imaging (DKI) and Neurite Orientation Dispersion and Density Imaging (NODDI) made available new tools to image axonal pathology non-invasively in vivo. These methods already showed greater sensitivity and specificity compared to conventional diffusion tensor-based metrics (e.g., fractional anisotropy), overcoming some of its limitations. While previous studies uncovered global and focal axonal degeneration in MS patients compared to healthy controls, here our aim is to investigate and compare different diffusion MRI acquisition protocols in their ability to highlight microstructural differences between MS and control tissue over several much used models. For comparison, we contrasted the ability of fractional anisotropy measurements to uncover differences between lesion, normal-appearing white matter (WM), gray matter and healthy tissue under the same imaging protocols. We show that: (1) focal and diffuse differences in several microstructural parameters are observed under clinical settings; (2) advanced models (CHARMED, DKI and NODDI) have increased specificity and sensitivity to neurodegeneration when compared to fractional anisotropy measurements; and (3) both high (3 T) and ultra-high fields (7 T) are viable options for imaging tissue change in MS lesions and normal appearing WM, while higher *b*-values are less beneficial under the tested short-time (10 min acquisition) conditions.

This article is part of a Special Issue entitled: *Non-invasive MRI Windows on Brain Inflammation*. © 2018 The Author(s). Published by Elsevier Ltd on behalf of IBRO. This is an open access article under the CC BY-NC-ND license (http://creativecommons.org/licenses/by-nc-nd/4.0/).

Key words: multiple sclerosis, multi-shell diffusion MRI, ultra-high field MRI, microstructure.

INTRODUCTION

Multiple sclerosis (MS) is a human neurological disorder with an onset most often in young adulthood that affects almost 2.5 million individuals worldwide, involving focal demyelination and axonal loss (Weinshenker, 1996; Noseworthy et al., 2000; Ellwardt and Zipp, 2014). With its ability to image soft tissues in vivo noninvasively, diffusion tensor imaging (DTI; Basser et al., 1994) has shown high sensitivity in detecting brain damage in MS. Using DTI, abnormalities in diffusivity patterns have been detected in focal MS lesions, normal-appearing white matter (NAWM) and gray matter (GM) (Werring et al., 1999; Vrenken et al., 2006). However, DTI-derived scalar indices such as fractional anisotropy (FA) (Basser and Pierpaoli, 1996) lack specificity to different sub-compartments of white matter (WM) microstructure: in the context of MS, both demyelination and axonal loss have similar impact on DTI indices and can therefore not be differentiated using this technique (Wheeler-Kingshott and Cercignani, 2011). In addition, it was

recently shown that DTI accuracy is strongly affected by the experimental parameters chosen, making it difficult to interpret and merge data coming from different centers (Barrio-Arranz et al., 2015).

In the last few years, several advanced diffusion-weighted imaging methods have been introduced to overcome these limitations. Diffusional Kurtosis Imaging (DKI) quantifies the deviation of the MRI signal decay from the DTI exponential model using a dimensionless metric called the excess kurtosis (Jensen et al., 2005). Recent evidence suggests that DKI indices like the mean kurtosis are affected in MS compared to controls (Guglielmetti et al., 2016). Moreover, significant correlations between DKI parameters and the Expanded Disability Status Scale were also reported (de Kouchkovsky et al., 2016). The Composite Hindered and Restricted Model of Diffusion (CHARMED) (Assaf et al., 2004) separates the contributions of different intra- and extracellular water compartments to the signal decay measured in diffusion-weighted imaging, and can therefore be used to extract new biomarkers of tissue microstructure which are able to disentangle the effects of axonal loss from those due to demyelination (Assaf et al., 2004). CHARMED generates maps of the restricted water fraction (FR), a proxy for the axonal density, which was recently shown to provide increased specificity and sensitivity to microstructural changes happening in early MS, both in lesions and in NAWM (De Santis et al., 2017). Along the same lines, Neurite Orientation Dispersion and Density Imaging (NODDI; Zhang et al., 2012) provides, in addition to the restricted water fraction, an index quantifying the fiber dispersion. A few recent studies used the NODDI model to investigate GM (Granberg et al., 2017), spinal cord (By et al., 2017) and WM (Granberg et al., 2017; Schneider et al., 2017), reporting an increase in both sensitivity and specificity in differentiating patients from controls.

The acquisition time for these advanced diffusion-weighted imaging methods is typically longer than for DTI, as they require the diffusion images to be acquired along many different gradient orientations and for at least two different b-values (Chuhutin et al., 2017; Zhang et al., 2012; De Santis et al., 2014), i.e., they need a multi-shell diffusion MRI acquisition. The majority of the mentioned studies were performed using advanced gradient equipment (i.e., maximum gradient intensity of 300 mT/m, De Santis et al., 2017); the same protocols implemented on scanners mounting conventional gradient equipment (40–80 mT/m) would result in acquisition times too long for the clinical setting to be feasible, and a drop in the signal-to-noise ratio. The remaining challenge for translation to clinics at 3 T, and for inclusion into advanced pipelines at 7 T, is to be able to measure these microstructural changes under more conventional gradient settings.

Employing an efficient pipeline is extremely important because it dramatically affects the accuracy and precision of the measured biomarkers. In the context of MS, improved accuracy and precision can potentially uncover early tissue changes invisible to conventional approaches. In addition, an optimal scheme can reduce the acquisition time, which is critical for ensuring feasibility of advanced diffusion MRI methods in clinical studies, possibly also in a multi-center design and, ultimately, to pave the way for their inclusion into clinical routine. However, this theme is often disregarded due to the high complexity of the model parameters optimization; a few studies have proposed optimal experimental designs for multi-shell techniques (Alexander et al., 2010; Prčkovska et al., 2012; Zhang et al., 2012; De Santis et al., 2014; Chuhutin et al., 2017), but these were not yet applied to MS patient studies. In addition, the differential ability of various diffusion-based imaging biomarkers to highlight microstructural abnormalities present in MS tissue compared to healthy controls has not yet been investigated.

Here, we employed two optimized multi-shell diffusion protocols at two different fields (7 T vs. 3 T) to measure several MRI biomarkers in a cohort of MS patients and a matched cohort of healthy controls, with the aim of identifying the protocol that best distinguishes tissue differences in lesions, NAWM and normal appearing gray matter (NAGM) compared to healthy controls. For the CHARMED model, the only tested model for which very high (> 3000 s/mm^2) b-values can be beneficial, two different acquisition protocols proposed in recent literature, at low (Zhang et al., 2012) and very high b-value (De Santis et al., 2014), were also tested.

This work is expected to impact future choices for investigating MS WM microstructure in larger cohorts, follow-ups or focusing on specific stages of the disease, and for selecting the appropriate experimental framework to obtain optimal data quality for the allocated time.

EXPERIMENTAL PROCEDURES

Data acquisition

Seven MS patients and six age-matched healthy controls underwent a comprehensive MRI protocol in two different sessions, scheduled no more than 48 h apart. All MS patients were in the early phase of the disease (duration ≤3 years) and had been diagnosed with relapsing-remitting MS. At the time of scanning, three were receiving medical treatment with interferon beta-1a, two with natalizumab, one with mitoxantrone and one with glatiramer acetate. Participants' demographic and clinical characteristics are reported in Table 1.

Table 1. Participants' demographic and clinical characteristics: mean number of lesions, mean disease duration in years and median EDSS. Abbreviations: MS = Multiple sclerosis; SD = Standard deviation; EDSS = Expanded Disability Status Scale

|	Mean age (SD)	Mean n of lesions	Mean disease duration (months)	Median EDSS
Healthy	42 (15) y	–	–	–
MS	42 (15) y	8.3 ± 6.5	21 ± 11	1 (range 0–3)
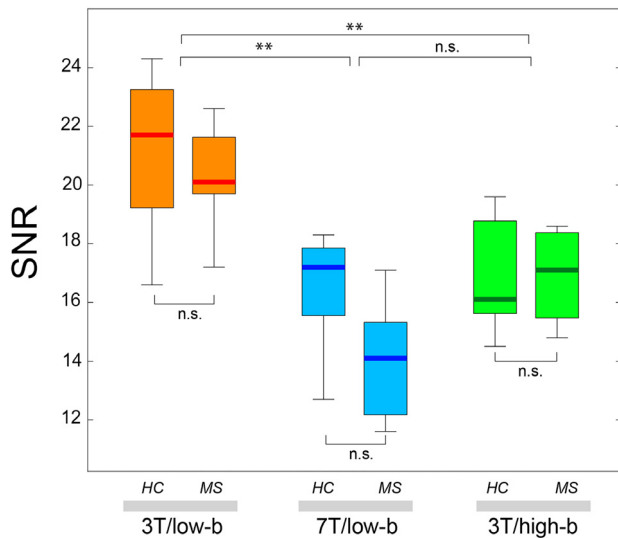
Fig. 1. Boxplot of SNR of the b0 image (unweighted scan) for the three different tested protocols, separated for the healthy control group and the MS patients. The bottom and top of the box are first and third quartiles, and the thick band inside the box is the median. Whiskers represent maximum and minimum of all data. Asterisks represent significant difference in the *t*-test statistic (** = $P < 0.01$). Abbreviations: HC = Healthy controls, MS = Multiple sclerosis; SNR = Signal-to-noise ratio.

The first scan session was acquired on a 3 T Siemens Prisma[FIT] scanner and comprised: an anatomical magnetization-prepared rapid gradient-echo (MPRAGE) scan, resolution 1 mm isotropic, TE/TR 2/2250 ms; a multi-shell diffusion protocol with $b = 700/2000$ s/mm^2 and 27/45 gradient orientations according to Zhang et al. (2012), plus two unweighted scans with forward phase encoding and six unweighted scans with reversed phase encoding, at 1.5-mm isotropic resolution, TE/TR 68/4873 ms, scan duration 8 min; and another multi-shell diffusion protocol with maximum b = 6000 s/mm^2, 106 unique gradient orientations distributed in eight shells of *b*-value between 750 and 6000 s/mm^2 according to De Santis et al. (2014), plus six unweighted scans with forward phase encoding and six unweighted scans with reversed phase encoding, at 1.5-mm isotropic resolution, TE/TR 94/6000 ms, scan duration 12 min. The Simultaneous multislice or Multiband (MB) acceleration technique (Setsompop et al., 2012), implemented in the Center for Magnetic Resonance Research (CMRR) (https://www.cmrr.umn.edu/multiband/), was used for all diffusion protocols with multiband factor 2 and generalized autocalibrating partial parallel acquisition (GRAPPA) factor 2 (Moeller et al., 2010; Xu et al., 2013). Throughout this work, the first multi-shell protocol will be addressed as "low-b protocol" while the second multi-shell protocol will be addressed as "high-b protocol". Total acquisition time was around 30 min.

The second session was acquired on a 7 T Magnetom Siemens scanner. To minimize the effects of B1 inhomogeneity, dielectric pads (Teeuwisse et al., 2012) were placed between the subject's head and the coil, positioned in correspondence with temporal and occipital
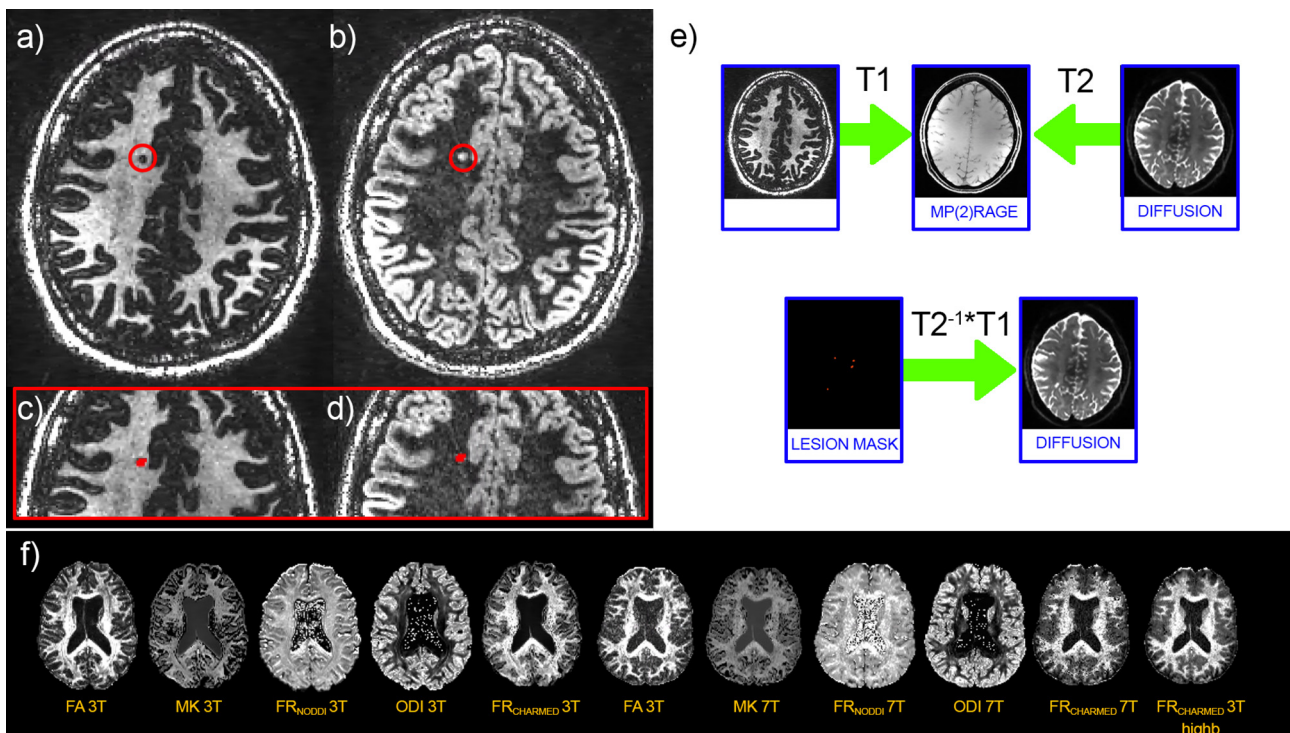
Fig. 2. Lesion mask on WM DIR (a) and GM DIR (b) maps. The lesion (circled in red) appears as a region of hypo-intensity in the WM DIR and hyper-intensity in the GM DIR. In panels (c) and (d), the lesion mask is shown. (e) Schematic of the registration procedure which brings lesion mask in diffusion space. (f) Example of microstructural maps employed in this study. Abbreviations: WM = White matter, DIR = Double Inversion Recovery; GM = Gray matter; FA = Fractional anisotropy; MK = Mean Kurtosis; FR = Restricted fraction; NODDI = Neurite orientation dispersion and density imaging; ODI = Orientation Dispersion Index; CHARMED = Composite hindered and restricted model of diffusion.

lobes, i.e., the brain areas most affected by such inhomogeneity in a volume transmit coil. The session comprised: an anatomical MP2RAGE scan, resolution 0.7 mm isotropic, TE/TR 2.47/5000 ms, scan duration 10 min; a multi-shell diffusion with $b = 700/2000$ s/mm^2 and 27/45 gradient orientations, plus two unweighted scans with forward phase encoding and six unweighted scans with reversed phase orientation, at 1.5-mm isotropic resolution, TE/TR 60/7500 ms, scan duration 10 min; a WM Double Inversion Recovery (DIR; Pracht et al., 2017) scan with resolution 1 mm isotropic, TE/TR 163/3000, scan duration 8 min; a GM DIR scan with resolution 1 mm isotropic, TE/TR 163/3000, scan duration 8 min. GRAPPA was used with factor 2. Total acquisition time, comprising also adjustment time, was around one hour. Due to the need to keep the examination time within one hour, and because of the higher penalty of long-TE high b-value diffusion scan (the relaxation time T_2 is shorter at higher fields) it was not possible to acquire a high-b diffusion protocol at 7 T.

Data processing and normalization

Diffusion data were pre-processed using FSL TOPUP and EDDY (Andersson et al., 2003; Andersson and Sotiropoulos, 2016) to correct for susceptibility-induced distortions, eddy currents and subject motion. Signal-to-Noise Ratio (SNR) values in the b0 images were calculated for each diffusion protocol in the whole brain using the difference method (Murphy et al., 1993), returning: SNR = 20.6 ± 2.2 for 3 T/low-b protocol, SNR = 15.1 ± 2.3 for 7 T/low-b protocol and SNR = 16.9 ± 1.7 for 3 T/high-b protocol. Boxplots of SNRs for the different protocols are shown in Fig. 1.

Conventional DTI data analysis was performed with the ExploreDTI software (Leemans et al., 2009) using only the $b = 700$ s/mm^2 shell; from the tensor, maps of FA were obtained. Only low-b protocols were used to estimate FA, since the DTI model is not appropriate for b-values > 1500 s/mm^2 (Jones et al., 1999).

Subsequently, all diffusion data at both fields was employed for multi-shell diffusion analysis. The kurtosis model was fitted using FSL's FDT (Jenkinson et al., 2012) to obtain the mean kurtosis (MK), while NODDI maps of restricted volume fraction (FR$_{NODDI}$) and orientation dispersion (ODI) were fitted using the software MDT (https://github.com/cbclab/MDT, version 0.10.6) using the Cascade Initialized optimization strategy (Harms et al., 2017). The CHARMED model was fitted using in-house software written in Matlab R2015b (The Mathworks). The CHARMED fitting procedure was based on nonlinear least square estimation using a Levenberg-Marquardt optimization. After fitting the CHARMED model, maps of the restricted volume fraction (FR$_{CHARMED}$) were computed for each subject under all the tested conditions: 3 T/low-b, 3 T/high-b and 7 T/low-b.

In the MS group, lesions were segmented manually and carefully checked by a trained radiologist using the two DIR images at 7 T, where the lesions are hyperintense in the GM-DIR and hypo-intense in the WM-DIR, as shown in Fig. 2. Lesions were only scored above 3 voxels in size based on at least 1 mm^2

Table 2. Mean values and standard deviations for all biomarkers and for all the tested protocols in WM skeleton, GM and lesions, compared to the corresponding values in the healthy cohort. Abbreviations: FA = Fractional anisotropy; MK = Mean Kurtosis; FR = Restricted fraction; NODDI = Neurite orientation dispersion and density imaging; ODI = Orientation Dispersion Index; CHARMED = Composite hindered and restricted model of diffusion; M = mean; SD = Standard deviation; HCWM = Healthy control white matter; NAWM = Normal appearing white matter; HCGM = Healthy control gray matter; NAGM = Normal appearing gray matter; HCLES = Healthy control in lesions; LES = Lesions; MS = Multiple sclerosis

	FA 3 T		FA 7 T		MK 3 T		MK 7 T		FR$_{NODDI}$ 3 T		FR$_{NODDI}$ 7 T		ODI 3 T		ODI 7 T		FR$_{CHARMED}$ 3 T		FR$_{CHARMED}$ 7 T		FR$_{CHARMED}$ 3 T high-b	
	M	SD	M	SD	M	SD	M	SD	M	SD	M	SD	M	SD	M	SD	M	SD	M	SD	M	SD
HCWM	0.59	0.11	0.69	0.08	0.98	0.13	0.87	0.19	0.46	0.10	0.51	0.12	0.16	0.07	0.16	0.09	0.53	0.06	0.54	0.07	0.47	0.08
NAWM	0.63	0.09	0.68	0.09	0.93	0.12	0.95	0.44	0.43	0.08	0.44	0.12	0.15	0.09	0.12	0.09	0.51	0.08	0.52	0.09	0.46	0.08
HCGM	0.25	0.06	0.27	0.06	0.69	0.18	0.69	0.19	0.43	0.07	0.44	0.08	0.31	0.09	0.31	0.08	0.21	0.13	0.27	0.07	0.23	0.08
NAGM	0.25	0.06	0.26	0.06	0.66	0.10	0.71	0.12	0.40	0.06	0.37	0.10	0.30	0.08	0.26	0.10	0.20	0.11	0.26	0.07	0.22	0.07
HCLES	0.39	0.06	0.44	0.07	0.92	0.09	0.96	0.06	0.50	0.03	0.54	0.036	0.25	0.03	0.23	0.04	0.40	0.06	0.45	0.05	0.38	0.06
LES	0.39	0.08	0.43	0.10	0.84	0.11	0.86	0.09	0.46	0.08	0.39	0.13	0.23	0.06	0.21	0.08	0.36	0.09	0.42	0.07	0.34	0.07

in-plane resolution, according to recent consensus recommendations (Geurts et al., 2011), but lesions smaller than 12 voxels in volume were not taken into account in the statistics, in order to forego possible co-registration inaccuracies. The lesion masks were then transferred into the diffusion space according to the following procedure: the WM DIR maps were registered to the MPRAGE maps (for 3 T) or to the MP2RAGE maps (for 7 T); then, the diffusion unweighted scans (i.e., b0s) were registered to the MPRAGE and MP2RAGE anatomical scans, and the inverse transformation was calculated. All the transformations employed at this stage were rigid body (6 degrees of freedom); the cost function chosen was the Correlation Ratio and all the brains were extracted using FSL BET software (Jenkinson and Smith, 2001) prior to registration. The two transformations were combined and applied to the lesion masks. All the aforementioned registration steps were performed using FSL FLIRT software (Jenkinson and Smith, 2001); the registration pipeline is illustrated in Fig. 2e.

All FA maps were then nonlinearly warped to the FMRIB58 FA template using ANTs (Klein et al., 2009). Importantly, the co-registration procedure excludes lesion masks from the computation of the figure of merit employed in the optimization procedure that calculates warp fields, so that the normalization is accurate also for MS subjects. The same transformation was applied to all the other biomarkers (MK, FR_{NODDI}, ODI, $FR_{CHARMED}$) and to the lesion masks.

To compare NAWM in MS patients and controls, the WM skeleton was calculated using parts of the TBSS pipeline (Smith et al., 2006) combined with an automatic ROI (region of interest) selection using WM labeling in standard space (JHU ICBM DTI 81 Atlas, also available in FSL), a procedure described previously (De Santis et al., 2012). To compare NAGM between MS patients and controls, a similar approach was employed using the GM parcellation in Brodmann areas available in ExploreDTI (Leemans et al., 2009).

Mean values and standard deviations were calculated for each parameter (MK, FR_{NODDI}, ODI, $FR_{CHARMED}$) and each protocol (3 T/low-b, 3 T/high-b and 7 T/low-b) in the following regions: (1) in each ROI belonging to the WM skeleton for controls and MS (in MS, lesions were excluded); (2) in each ROI belonging to the GM parcellation for controls and MS (in MS, lesions were excluded); and 3) in each lesion from the masks for MS patients and in the corresponding registered ROI from healthy controls.

Statistical analysis

Analysis of variance (ANOVA) was used to assess whether the applied protocol had a significant effect on the measured parameters. Within-subject effect was the protocol (3 T and 7 T for FA, MK, FR_{NODDI}, ODI and 3 T/low-b, 3 T/high-b and 7 T/low-b for $FR_{CHARMED}$) and between-subject effect was the tissue kind (healthy, NAWM, NAGM, lesion). SNR was included as covariate of no interest in the analysis.

Given that different anatomical locations present different baseline values for each parameter, in order to render differences between MS lesions and corresponding ROIs in healthy controls comparable, we calculated the difference between the two values and divided it by the reference value in healthy controls, according to the following formula:

$$P_{NORM} = (P_{MS\ lesion\ mask} - P_{healthy\ lesion\ mask})/P_{healthy\ lesion\ mask}$$

where P is the parameter (FA, MK, FR_{NODDI}, ODI, $FR_{CHARMED}$ in this study). The null hypothesis of no difference between lesions and healthy tissue was then tested across patients through a nonparametric signed-rank test. Likewise, the group effect was tested in 50 ROIs from the JHU ICBM DTI 81 atlas (Mori et al., 2008), projected onto the WM skeleton, using a non-parametric signed-rank test, and on 41 Brodmann areas in GM. The effect size was calculated as the difference between the biomarker values in the MS group and in the healthy control group, divided by the pooled standard deviation (Cohen's d). Post-hoc comparisons between groups were performed using the Mann–Whitney test, under the assumption that the presence of the disease causes a decrease in the measured imaging parameters (left tail only). Multiple comparisons were corrected for the false discovery rate (Benjamini and Yekutieli, 2005). All statistical analysis was performed with SPSS software (IBM SPSS Statistics for Mac, Version 23.0) and Matlab. P-values below 0.05 were considered significant.

RESULTS

Mean biomarker values and ANOVA

Mean values and standard deviations for the investigated biomarkers, in the whole WM skeleton, in the GM areas and in the lesion masks, are reported in Table 2.

In Table 3, the results of the ANOVA show that there is a significant effect of the type of tissue (lesion in MS, NAWM and WM in healthy controls) for all parameters,

Table 3. ANOVA results (F statistics and corresponding P-values) showing the effects of the protocol, of the tissue type, and of their interaction, on the measured biomarkers. Abbreviations: ANOVA = Analysis of variance, FA = Fractional anisotropy; MK = Mean Kurtosis; FR = Restricted fraction; NODDI = Neurite orientation dispersion and density imaging; ODI = Orientation Dispersion Index; CHARMED = Composite hindered and restricted model of diffusion

	FA		MK		FR_{NODDI}		ODI		$FR_{CHARMED}$	
	F	p-value	F	p-value	F	p-value	F	p-value	F	p-value
Protocol	11.6	< 0.01**	0.057	n.s.	5.1	< 0.05*	0.1	n.s.	5.3	< 0.05*
Tissue	125.8	< 0.01**	46.3	< 0.01**	16.3	< 0.01**	83.8	< 0.01**	9.4	< 0.01**
Interaction	4.5	< 0.01**	1.8	n.s.	0.2	n.s.	1.4	n.s.	24.1	< 0.01**
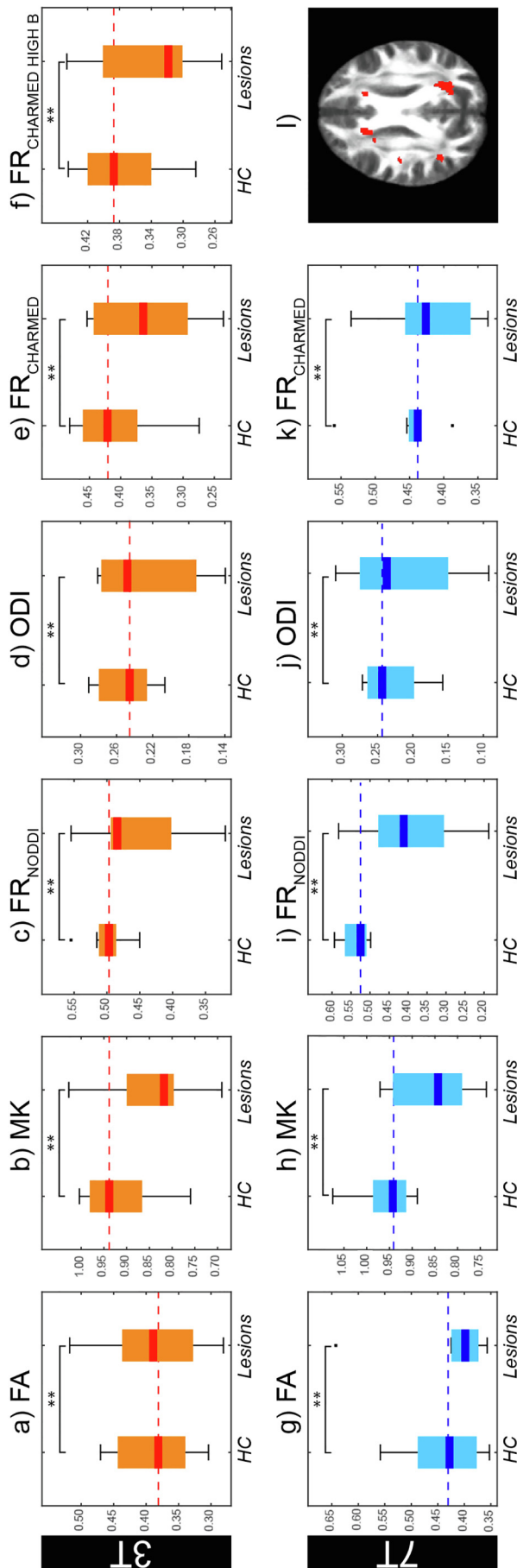
Fig. 3. In the top row, microstructural parameter values for healthy controls vs lesions measured at 3 T: FA (a), MK (b), FR from NODDI (c), ODI (d), FR from CHARMED (e) and FR from CHARMED measured with the high-b protocol (f). In the bottom row, microstructural parameter values for healthy controls vs lesions measured at 7 T: FA (g), MK (h), FR from NODDI (i), ODI (j), FR from CHARMED (k). Asterisks represent significant difference in the nonparametric signed-rank test statistic (** = P < 0.01). In (l), an example of lesion mask. Abbreviations: FA = Fractional anisotropy; MK = Mean Kurtosis; FR = Restricted fraction; NODDI = Neurite orientation dispersion and density imaging; ODI = Orientation Dispersion Index; CHARMED = Composite hindered and restricted model of diffusion; HC = Healthy controls.

while the protocol has a significant effect for FA, FR_{NODDI} and $FR_{CHARMED}$. The interaction between the two factors is significant for FA and $FR_{CHARMED}$.

Differences between MS lesions and healthy control tissue

Fig. 3 shows the values of FA, MK, FR_{NODDI}, ODI and $FR_{CHARMED}$ in lesions and in the corresponding healthy tissue in the control cohort across the different tested protocols; in the boxplot, the reported statistic indicates significant differences between the two cohorts in the nonparametric signed-rank test. All indices show significant differences for both tested protocols. Lesions, as expected, are characterized by higher standard deviation compared to control values.

Differences between NAWM and healthy control tissue

All indices show significant differences between NAWM and the corresponding healthy tissue in the control cohort at 3 T except ODI, while FA, ODI and FR from CHARMED and FR from NODDI show significant differences at 7 T. The boxplots and the corresponding nonparametric signed-rank test statistics are reported in Fig. 4.

Differences between NAGM and healthy control tissue

In NAGM, MK, ODI, FR from NODDI and FR from CHARMED at high-b show significant differences between healthy controls and MS at 3 T, while at 7 T only FA, FR from NODDI and ODI show significant differences between the two cohorts. The boxplots and the corresponding nonparametric signed-rank test statistics are reported in Fig. 5.

Effect size

The effect size, for all microstructural parameters and across the tested protocols, for the combinations with statistically significant decrease according to the post hoc test, is reported in Table 4. Notably, none of the differences found in the ANOVA for FA survive the post hoc t-test, while several microstructural indices show significant differences between healthy and MS cohort, with effect size up to 1.25. FR from CHARMED shows a clear pattern of reduction in MS compared to controls, both in lesions and NAWM, while no significant differences are found in NAGM. FR from NODDI shows a similar pattern, except the difference in NAWM at 7 T is not significant. Also MK shows reduction in MS compared to controls, in lesions, NAWM and NAGM at 3 T and only in lesions at 7 T. Notwithstanding the decreasing
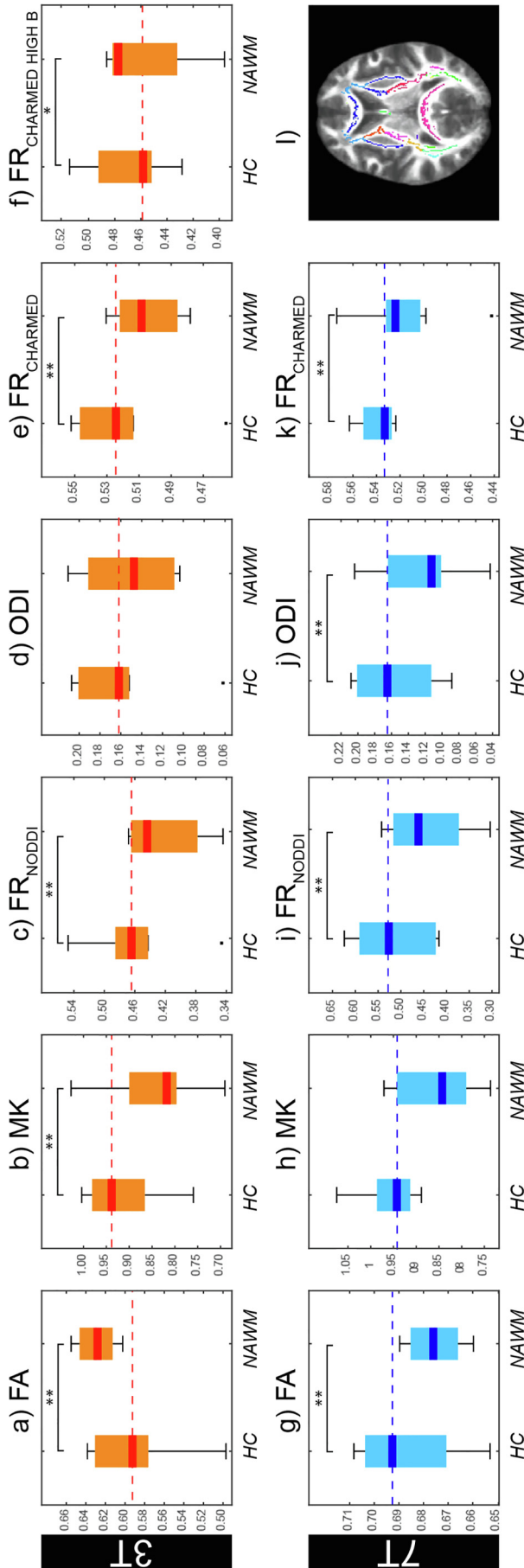
Fig. 4. In the top row, microstructural parameter values for healthy controls vs MS in NAWM measured at 3 T: FA (a), MK (b), FR from NODDI (c), ODI (d), FR from CHARMED (e) and FR from CHARMED measured with the high-b protocol (f). In the bottom row, microstructural parameter values for healthy controls vs MS in NAWM measured at 7 T: FA (g), MK (h), FR from NODDI (i), ODI (j), FR from CHARMED (k). Asterisks represent significant difference in the nonparametric signed-rank test statistic (* = $P < 0.05$, ** = $P < 0.01$). In (l), WM skeleton mask in which each ROI has a different color. Abbreviations: FA = Fractional anisotropy; MK = Mean Kurtosis; FR = Restricted fraction; NODDI = Neurite orientation dispersion and density imaging; ODI = Orientation Dispersion Index; CHARMED = Composite hindered and restricted model of diffusion; HC = Healthy controls; NAWM = Normal appearing white matter.

trend observed in the boxplot for MS versus controls, none of the significant difference in ODI survives post hoc *t*-test.

DISCUSSION

In this work, we employed three different multishell diffusion MRI protocols at two field strengths to measure five microstructural MRI parameters from a range of models (FA, MK, FR_{NODDI}, ODI and $FR_{CHARMED}$) in a cohort of MS patients and a matched cohort of healthy controls, with the aim of identifying the protocol and the biomarker that best mirrors tissue differences in the inflammatory lesions, in NAWM and NAGM compared to healthy controls.

The first result, replicating recent findings obtained in a high-end set-up (De Santis et al., 2017), is that under clinical settings more sophisticated microstructural measures ($FR_{CHARMED}$, FR_{NODDI}, and MK) are a better descriptor than FA for the underlying tissue alterations in both lesions and NAWM. The fact that $FR_{CHARMED}$, FR_{NODDI}, and MK differences are significant also in the relatively small cohort analyzed in this study adds to the translational potential of these multi-shell methods for the clinical routine. Interestingly, while there are no major differences between the performances of the low *b*-value protocols across fields, our results suggest that the short-time high *b*-value protocol is not optimal for microstructural analysis in MS. Furthermore, we show that a 10-min multishell diffusion protocol at 7 T has similar performance in MS when compared to its counterpart at 3 T, which is commonly considered the best option. There are no differences in $FR_{CHARMED}$ between NAGM and corresponding GM areas; this is expected as the model is specifically formulated to account for the geometry of WM.

FR_{NODDI} gives similar results as $FR_{CHARMED}$, although the differences for FR_{NODDI} in NAWM are not significant at 7 T. ODI gives complementary information about the neurite dispersion in both GM and WM and it has been proposed as a novel tool to capture microstructural changes in both NAWM and lesions in MS (Schneider et al., 2017). Increased ODI in NAWM and decreased ODI in lesions were reported in a small cohort (Schneider et al., 2017), but another larger study found no differences in normal-appearing tissue and an increase in lesions (Granberg et al., 2017). Here, we found a trend of reduced ODI in both MS WM and GM compared to controls, which however is not statistically significant. Taken together, these results suggest that more studies with larger cohorts are needed to characterize the ODI as a putative marker for MS.

MK is reduced in MS compared to controls in lesions, NAWM and NAGM at 3 T, and only in lesions at 7 T. The reduction of MK in MS tissue compared to controls is in agreement with recent
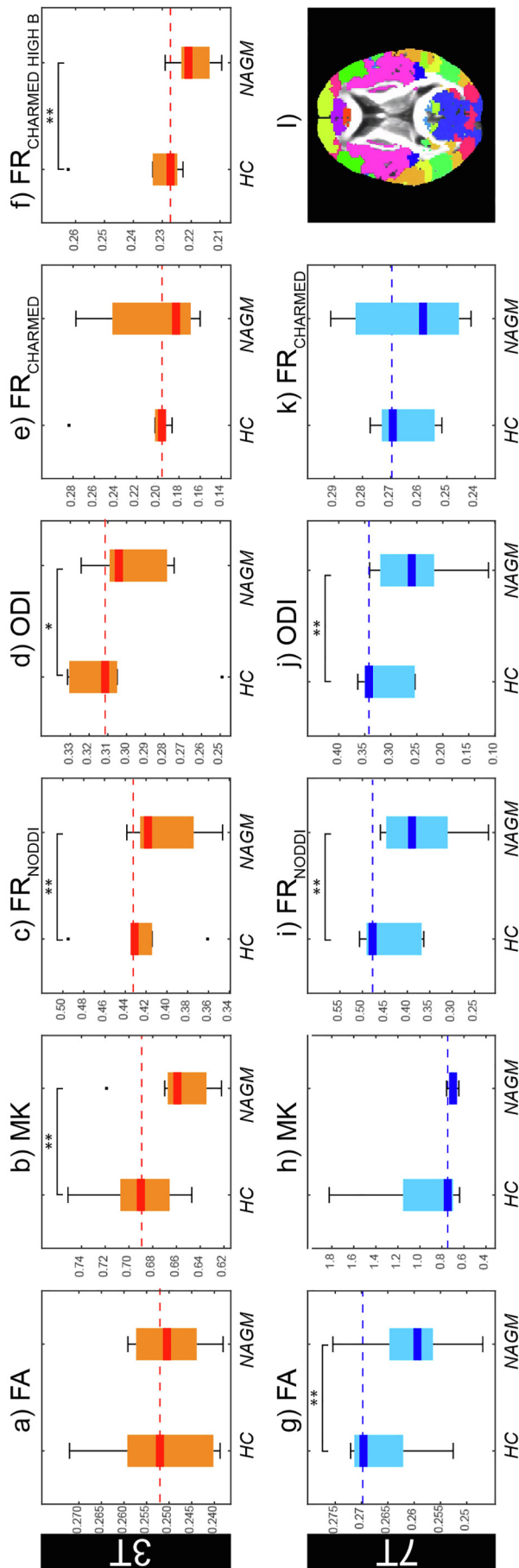
Fig. 5. In the top row, microstructural parameter values for healthy controls vs MS in NAGM measured at 3 T: FA (a), MK (b), FR from NODDI (c), ODI (d), FR from CHARMED (e) and FR from CHARMED measured with the high-b protocol (f). In the bottom row, microstructural parameter values for healthy controls vs MS in NAGM measured at 7 T: FA (g), MK (h), FR from NODDI (i), ODI (j), FR from CHARMED (k). Asterisks represent significant difference in the nonparametric signed-rank test statistic (** = P < 0.01). In (l), GM areas skeleton mask in which each ROI has a different color. Abbreviations: FA = Fractional anisotropy; MK = Mean Kurtosis; FR = Restricted fraction; NODDI = Neurite orientation dispersion and density imaging; ODI = Orientation Dispersion Index; CHARMED = Composite hindered and restricted model of diffusion; HC = Healthy controls; NAGM = Normal appearing gray matter.

work (Guglielmetti et al., 2016; Qian et al., 2016). Recent findings (Chuhutin et al., 2017) highlighted that precision and accuracy on MK are highly dependent on the proper choice of *b*-values; the ones employed in this study are optimal for WM, but suboptimal for GM. Repeating the experiment using a protocol with lower *b*-value might provide further insights into the differences in kurtosis in NAGM compared to controls.

The effect size in lesions, as expected, is always larger compared to NAWM and NAGM. Nonetheless, most of the multi-shell microstructural parameters show differences in NAWM, and some also in NAGM, while FA does not capture significant differences. While the lack of results using conventional DTI might be certainly due to the relatively small cohort employed in this study, or to the choice of *b*-value, it is important to note that multi-shell diffusion imaging has enough sensitivity to highlight differences between healthy and lesioned tissue also with low sample sizes, with huge potential for the clinical routine.

The main differences between the different tested protocols are: (1) the SNR of the images, affected by both the field magnitude and the echo time; (2) the diffusion contrast, which depends on the applied *b*-value; and (3) the echo time, which can change the proportion between tissue compartments with different T_2 relaxation times (De Santis et al., 2016).

There are differences between the SNRs across protocols, but these do not fully explain the results obtained: for example, the 3 T/high-*b* protocol does not have the lowest SNR, but showed the worst performance in detecting lesions and NAWM changes compared to the other protocols for $FR_{CHARMED}$. Moreover, when SNR is used as covariate in the ANOVA, the effect of the protocol is still significant for both FA, FR_{NODDI} and $FR_{CHARMED}$. Atrophy, demyelination and brain lesions can have an impact on the SNR, because they lead to changes in intensities and contrast, but the SNR was not different between the MS and control groups in any of the investigated protocols. The 3 T/low-*b* and 7 T/low-*b* protocols implemented in this study have the same *b*-value and similar timing in the diffusion sequence, implying similar diffusion and T_2 weighting; on the other hand, the 3 T/high-*b* sequence, having a larger maximum *b*-value and larger TE, also corresponds to different diffusion and T_2 weighting. The characteristics of the applied gradients influence the sensitivity of the sequence to different compartments; while normally high *b*-values are considered beneficial, for example, to increase the power to resolve fiber crossing (Cohen-Adad et al., 2011; De Santis et al., 2014), the results obtained here suggest that in the context of early-stage MS they may not be the best choice. We speculate that this might depend on

Table 4. Effect size (Cohen's *d*) of the difference between healthy control and MS in lesions, NAWM and NAGM at both field strengths (3 T and 7 T) for all the microstructural parameters: FA, MK, FR from NODDI, ODI, FR from CHARMED and FR from CHARMED measured with the high-b protocol. Asterisks represent significant difference in the Mann–Whitney test statistic (* = P < 0.05, ** = P < 0.01). Abbreviations: FA = Fractional anisotropy; MK = Mean Kurtosis; FR = Restricted fraction; NODDI = Neurite Orientation Dispersion and Density Imaging; ODI = Orientation Dispersion Index; CHARMED = Composite Hindered and Restricted Model of Diffusion; NAWM = Normal-appearing white matter; NAGM = Normal-appearing gray matter

	3 T			7 T		
	Lesions	NAWM	NAGM	Lesions	NAWM	NAGM
FA	n.s.	n.s.	n.s.	n.s.	n.s.	n.s.
MK	−0.78	−0.90	−0.93	−1.00	n.s.	n.s.
FR$_{NODDI}$	−0.80	−0.95	n.s.	−1.25	n.s.	n.s.
ODI	n.s.	n.s.	n.s.	n.s.	n.s.	n.s.
FR$_{CHARMED}$	−0.74	−0.95	n.s.	−0.64	−0.67	n.s.
FR$_{CHARMED\ HIGHB}$	−0.60	n.s.	−0.99	–	–	–

inflammation-related differences in the T_2 relaxation time between normal and damaged tissue (van Waesberghe et al., 1999), given that a long echo time (required for high *b*-values on clinical gradients) changes the proportion between tissue compartments with different T_2 relaxation times (De Santis et al., 2016). The situation can be different for more advanced configurations, like gradients with intensity even higher than 70–80 mT/m, which achieve a TE reduction for high *b*-values, for long-time protocols, or for further advances which significantly increase the speed of imaging. Our results also suggest that the high *b*-value protocol can be useful when looking at GM.

Importantly, our findings support the feasibility of CHARMED, NODDI and DKI at 7 T. With the numerous further advantages in other (e.g., functional) MRI imaging contrasts, ultra-high field is rapidly emerging as the high-end instrument for neuroimaging. 7 T is sometimes considered to be of limited benefit for diffusion, but recent studies demonstrated that SNR differences across similar diffusion protocols at 3 T and 7 T are minimal (Wen et al., 2015), and that 7 T can even be advantageous when high gradient intensity (i.e., > 70 mT/m) is available (Uğurbil et al., 2013). The results presented here might also contribute to explaining the discrepancy in the findings of different diffusion MRI studies in MS, which can be at least partially attributed to differences in the protocols used, and lay the ground for the standardization of diffusion protocols in MS.

Multi-shell diffusion acquisitions increased the ability to detect axonal pathology occurring in MS brain tissue compared to conventional DTI in a small pilot study, also under clinical settings. In addition, our findings suggest that multi-shell diffusion MRI at both high (3 T) and ultra-high fields (7 T) are viable options for imaging tissue change in MS lesions and normal appearing WM, while higher *b*-values are not beneficial for MS under the tested short-time (10 min acquisition) conditions.

REFERENCES

Alexander DC, Hubbard PL, Hall MG, Moore EA, Ptito M, Parker GJ, Dyrby TB (2010) Orientationally invariant indices of axon diameter and density from diffusion MRI. NeuroImage 52(4):1374–1389.

Andersson JLR, Sotiropoulos SN (2016) An integrated approach to correction for off-resonance effects and subject movement in diffusion MR imaging. NeuroImage 125:1063–1078.

Andersson JLR, Skare S, Ashburner J (2003) How to correct susceptibility distortions in spin-echo echo-planar images: application to diffusion tensor imaging. NeuroImage 20(2):870–888.

Assaf Y, Freidlin RZ, Rohde GK, Basser PJ (2004) New modeling and experimental framework to characterize hindered and restricted water diffusion in brain white matter. Magn Reson Med 52(5):965–978.

Basser PJ, Pierpaoli C (1996) Microstructural and physiological features of tissues elucidated by quantitative-diffusion-tensor MRI. J Magn Reson B 111(3):209–219.

Basser PJ, Mattiello J, LeBihan D (1994) Estimation of the effective self-diffusion tensor from the NMR spin echo. J Magn Reson B 103(3):247–254.

Benjamini Y, Yekutieli D (2005) False discovery rate: adjusted multiple confidence intervals for selected parameters. J Am Stat Assoc 100(469):71–81.

By S, Xu J, Box BA, Bagnato FR, Smith SA (2017) Application and evaluation of NODDI in the cervical spinal cord of multiple sclerosis patients. Neuroimage Clin 15:333–334.

Chuhutin A, Hansen B, Jespersen SN (2017) Precision and accuracy of diffusion kurtosis estimation and the influence of *b*-value selection. NMR Biomed 30(11).

Cohen-Adad J, Descoteaux M, Wald LL (2011) Quality assessment of High Angular Resolution Diffusion Imaging data using bootstrap on Q-ball reconstruction. J Magn Reson Imaging 33(5): 1194–1208.

de Kouchkovsky I, Fieremans E, Fleysher L, Herbert J, Grossman RI, Inglese M (2016) Quantification of normal-appearing white matter tract integrity in multiple sclerosis: a diffusion kurtosis imaging study. J Neurol. 263(6):1146–1155.

De Santis S, Assaf Y, Jones DK (2012) Using the biophysical CHARMED model to elucidate the underpinnings of contrast in

diffusional kurtosis analysis of diffusion-weighted MRI. Magn Reson Mater Phys 25:267–276.

De Santis S, Assaf Y, Evans CJ, Jones DK (2014) Improved precision in CHARMED assessment of white matter through sampling scheme optimization and model parsimony testing. Magn Reson Med 71:661–671.

De Santis S, Granberg T, Ouellette R, Treaba CA, Fan Q, Herranz E, Mainero C, Toschi N (2017), Early axonal damage in normal appearing white matter in Multiple Sclerosis: novel insights from multi-shell diffusion MRI. In: 39th Annual International Conference of the IEEE Engineering in Medicine and Biology Society (EMBC).

De Santis S, Assaf Y, Jones DK (2016). The influence of T2 relaxation in measuring the restricted volume fraction in diffusion MRI. In: Proceedings of the 24th Scientific Meeting, International Society for Magnetic Resonance in Medicine, Singapore, abstract n. 1998.

Ellwardt E, Zipp F (2014) Molecular mechanisms linking neuroinflammation and neurodegeneration in MS. Exp Neurol 262:8–17.

Geurts JJ, Roosendaal SD, Calabrese M, Ciccarelli O, Agosta F, Chard DT, Gass A, Huerga E, Moraal B, Pareto D, Rocca MA, Wattjes MP, Yousry TA, Uitdehaag BM, Barkhof F, MAGNIMS Study Group (2011) Consensus recommendations for MS cortical lesion scoring using double inversion recovery MRI. Neurology 76 (5):418–424.

Granberg T, Fan Q, Treaba CA, Ouellette R, Herranz E, Mangeat G, et al. (2017). Brain 140:2912–2926.

Guglielmetti C, Veraart J, Roelant E, Mai Z, Daans J, Van Audekerke J, Naeyaert M, Vanhoutte G, Delgado y Palacios R, Praet J, Fieremans E, Ponsaerts P, Sijbers J, Van der Linden A, Verhoye M (2016) Diffusion kurtosis imaging probes cortical alterations and white matter pathology following cuprizone induced demyelination and spontaneous remyelination. NeuroImage 125:363–377.

Harms RL, Fritz FJ, Tobisch A, Goebel R, Roebroeck A (2017) Robust and fast nonlinear optimization of diffusion MRI microstructure models. Neuroimage 15(155):82–96.

Jenkinson M, Smith SM (2001) A global optimisation method for robust affine registration of brain images. Med Image Anal 5 (2):143–156.

Jensen JH, Helpern JA, Ramani A, Lu H, Kaczynski K (2005) Diffusional kurtosis imaging: the quantification of non-gaussian water diffusion by means of magnetic resonance imaging. Magn Reson Med 53(6):1432–1440.

Jones DK, Horsfield MA, Simmons A (1999) Optimal strategies for measuring diffusion in anisotropic systems by magnetic resonance imaging. Magn Reson Med 42:515–525.

Klein A, Andersson J, Ardekani BA, Ashburner J, Avants B, Chiang MC, Christensen GE, Collins DL, Gee J, Hellier P, Song JH, Jenkinson M, Lepage C, Rueckert D, Thompson P, Vercauteren T, Woods RP, Mann JJ, Parsey RV (2009) Evaluation of 14 nonlinear deformation algorithms applied to human brain MRI registration. Neuroimage 46:786–802.

Leemans A, Jeurissen B, Sijbers J, Jones DK (2009). ExploreDTI: a graphical toolbox for processing, analyzing, and visualizing diffusion MR data. In: Proceedings of the 17th Scientific Meeting, International Society for Magnetic Resonance in Medicine, Honolulu, USA, abstract n. 3537.

Moeller S, Yacoub E, Olman CA, Auerbach E, Strupp J, Harel N, Uğurbil K (2010) Multiband multislice GE-EPI at 7 Tesla, with 16-fold acceleration using partial parallel imaging with application to high spatial and temporal whole-brain fMRI. Magn Reson Med 63 (5):1144–1153.

Mori S, Oishi K, Jiang H, Jiang L, Li X, Akhter K, Hua K, Faria AV, Mahmood A, Woods R, Toga AW, Pike GB, Neto PR, Evans A, Zhang J, Huang H, Miller MI, van Zijl P, Mazziotta J (2008) Stereotaxic white matter atlas based on diffusion tensor imaging in an ICBM template. Neuroimage 40(2):570–582.

Murphy BW, Carson PL, Ellis JH, Zhang YT, Hyde RJ, Chenevert TL (1993) Signal-to-noise measures for magnetic resonance imagers. Magn Reson Imaging 11(3):425–428.

Noseworthy JH, Lucchinetti C, Rodriguez M, Weinshenker BG (2000) Multiple sclerosis. N Engl J Med 343:938–952.

Pracht ED, Feiweier T, Ehses P, Brenner D, Roebroeck A, Weber B, Stöcker T (2017) SAR and scan-time optimized 3D whole-brain double inversion recovery imaging at 7T. Magn Reson Med (in press). https://doi.org/10.1002/mrm.26913.

Prčkovska V, Achterberg HC, Bastiani M, Pullens P, Balmashnova E, Ter Haar Romeny BM, Vilanova A, Roebroeck A (2012) Optimal short-time acquisition schemes in high angular resolution diffusion-weighted imaging. Int J Biomed Imaging 2013(2013):658583.

Qian W, Chan KH, Hui ES, Lee CY, Hu Y, Mak HK (2016) Application of diffusional kurtosis imaging to detect occult brain damage in multiple sclerosis and neuromyelitis optica. NMR Biomed 29:1536–1545.

Schneider T, Brownlee W, Zhang H, Ciccarelli O, Miller DH, Wheeler-Kingshott CG (2017) Sensitivity of multi-shell NODDI to multiple sclerosis white matter changes: a pilot study. Funct Neurol 32:97–101.

Setsompop K, Cohen-Adad J, Gagoski BA, Raij T, Yendiki A, Keil B, Wedeen VJ, Wald LL (2012) Improving diffusion MRI using simultaneous multi-slice echo planar imaging. Neuroimage 15 (63):569–580.

Smith SM, Jenkinson J, Johansen-Berg H, Rueckert D, Nichols TE, Mackay CE, Watkins KE, Ciccarelli O, Cader MZ, Matthews PM, Behrens TE (2006) Tract-based spatial statistics: voxelwise analysis of multi-subject diffusion data. NeuroImage 31: 1487–1505.

Teeuwisse WM, Brink WM, Haines KN, Webb AG (2012) Simulations of high permittivity materials for 7 T neuroimaging and evaluation of a new barium titanate-based dielectric. Magn Reson Med 67 (4):912–918.

Uğurbil K, Xu J, Auerbach EJ, Moeller S, Vu AT, Duarte-Carvajalino JM, Lenglet C, Wu X, Schmitter S, Van de Moortele PF, Strupp J, Sapiro G, De Martino F, Wang D, Harel N, Garwood M, Chen L, Feinberg DA, Smith SM, Miller KL, Sotiropoulos SN, Jbabdi S, Andersson JL, Behrens TE, Glasser MF, Van Essen DC, Yacoub E, WU-Minn HCP Consortium (2013) Pushing spatial and temporal resolution for functional and diffusion MRI in the Human Connectome Project. Neuroimage 80:80–104.

van Waesberghe JH, Kamphorst W, De Groot CJ, van Walderveen MA, Castelijns JA, Ravid R, Lycklama à Nijeholt GJ, van der Valk P, Polman CH, Thompson AJ, Barkhof F (1999) Axonal loss in multiple sclerosis lesions: magnetic resonance imaging insights into substrates of disability. Ann Neurol 46(5):747–754.

Vrenken H, Pouwels PJ, Geurts JJ, Knol DL, Polman CH, Barkhof F, Castelijns JA (2006) Altered diffusion tensor in multiple sclerosis normal-appearing brain tissue: cortical diffusion changes seem related to clinical deterioration. J Magn Reson Imaging 23 (5):628–636.

Weinshenker BG (1996) Epidemiology of multiple sclerosis. Neurol Clin 14:291–308.

Wen Q, Kelley DA, Banerjee S, Lupo JM, Chang SM, Xu D, Hess CP, Nelson SJ (2015) Clinically feasible NODDI characterization of glioma using multiband EPI at 7 T. Neuroimage Clin 9:291–299.

Werring DJ, Clark CA, Barker GJ, Thompson AJ, Miller DH (1999) Diffusion tensor imaging of lesions and normal-appearing white matter in multiple sclerosis. Neurology 12(8):1626–1632.

Xu J, Moeller S, Auerbach EJ, Strupp J, Smith SM, Feinberg DA, Yacoub E, Uğurbil K (2013) Evaluation of slice accelerations using multiband echo planar imaging at 3 T. Neuroimage 83:991–1001.

Zhang H, Schneider T, Wheeler-Kingshott CA, Alexander DC (2012) NODDI: practical in vivo neurite orientation dispersion and density imaging of the human brain. Neuroimage 61(4):1000–1016.